

Nanoscale structures in cleavage process of silicon on the basis of large-scale electronic structure calculation; surface reconstruction, anisotropy, step and bending.

Takeo Hoshi, Yusuke Iguchi, and Takeo Fujiwara

Department of Applied Physics, University of Tokyo, Bunkyo-ku, Tokyo 113-8656, Japan

(Dated: October 26, 2019)

The 10 nm scale structure in cleavage process of silicon is investigated, on the basis of the large-scale electronic structure calculation. Discussions are focused mainly on the unstable (001) cleavage process and the stable (experimentally observed) (111)-(2 \times 1) cleavage process. Surface reconstruction and step formation are observed and compared with experiments. These processes are analyzed by the quantum mechanical freedoms of electron system. The relative stability among the cleavage planes is presented as bendings of cleavage path into the favorite planes. These structural properties are understood by the competitive mechanism between the anisotropic strain field due to the global (crack) shape and the electronic structure with the crystalline symmetry. Moreover, several common aspects between cleavage and other phenomena are discussed from the viewpoints of non-equilibrium process and 10 nm scale structure.

PACS numbers: 71.15.Pd, 68.35.-p, 62.20.Mk

I. INTRODUCTION

Cleavage is a non-equilibrium process and the dynamics is essential. Especially, the cleavage of silicon single crystal is of great interest from the multiscale viewpoint between macroscale and atomscale pictures; In the macroscale picture, silicon shows perfect brittleness. In general, brittle fracture is mainly described by the continuum mechanics.^{1,2,3} See Appendix A for a brief explanation. In the atomscale picture, on the other hand, a cleaved surface contains areas with well-defined reconstructions. Nowadays, these atomscale structures are observed by scanning tunneling microscopy (STM)⁴ and other experiments. The multiscale feature of the phenomenon appears, as discussed in this paper, in atomistic processes within a nanoscale (or 10 nm scale) region near the crack tip, though such processes cannot be seen by a direct (*in situ*) experimental observation.

A simple but fundamental question is what Miller index and surface reconstruction appear as cleavage surface in semiconductor? A naive prediction is that the cleavage plane should be that with the smallest surface energy, or the smallest energy loss with forming surface. The naive prediction, however, is not always satisfactory, since cleavage is a non-equilibrium process. For example, the easiest cleavage surface of silicon is the (111)-(2 \times 1) structure,^{4,5,6,7,8,9,10} though the calculated surface energy of the (2 \times 1) structure is larger than that of the ground state (7 \times 7) structure.¹¹ The (2 \times 1) structure is metastable and will change, irreversibly, to the (7 \times 7) structure at finite temperatures.^{4,12}

Moreover, there are several interesting experimental facts; (i) The (110) cleavage plane is also experimentally observed but is less favorable than the (111) cleavage plane. Experimental STM images are found in Ref.¹³ See also a recent theoretical work¹⁴ and references therein. (ii) The cleaved Ge(111) surface also shows the same (2 \times 1) structure, while the ground state surface structure is not the (7 \times 7) structure but the c(2 \times 8) structure.^{4,11}

These facts should be considered, when we try to understand the cleavage mechanism of silicon.

In the present paper, the cleavage process will be investigated by molecular dynamics (MD) simulations on the basis of the large-scale electronic structure calculation method that has been developed recently.^{15,16,17,18,19,20} The results will be analyzed from the electronic freedoms and compared with experiments. This paper is organized as follows: Section II describes the important aspects of cleavage that will be discussed with the simulation results. The methodology of the present simulation is reviewed in Section III. In Section IV, the instability of the (001) cleavage mode is discussed, which will be compared with the (111) cleavage mode. The stable mode on the (111) plane is discussed in Section V and Section VI. In the latter section, step formations are focused. The simulation results with bendings in cleavage path are presented in Section VII. Finally, in Section VIII, we will find several common theoretical aspects on nanoscale structures between the cleavage process and other processes.

II. ASPECTS OF CLEAVAGE PROCESS IN REAL CRYSTAL

A. Non-equilibrium and quantum mechanical aspects

Cleavage phenomena, as a non-equilibrium process, has a typical time scale determined by the cleavage propagation velocity. In the continuum mechanics and many experiments, the propagation velocity is given on the order of, but less than, the sound velocity or the Rayleigh wave velocity ($v_R = 4.5\text{km/s} = 4.5\text{nm/ps}$ for Si).^{2,3} Therefore, the elementary atomistic process occurs within the time scale. Such a process is illustrated in Fig. 1(a)-(c), in which bond breakings and surface reconstructions occurs successively within the time scale of

cleavage propagation. Here the surface reconstruction is described schematically as dimerization. These processes are ‘fast’ and almost free from thermal equilibration. In the present context, annealing gives ‘slow’ reconstruction processes to reach the thermodynamic ground state of surface structure.

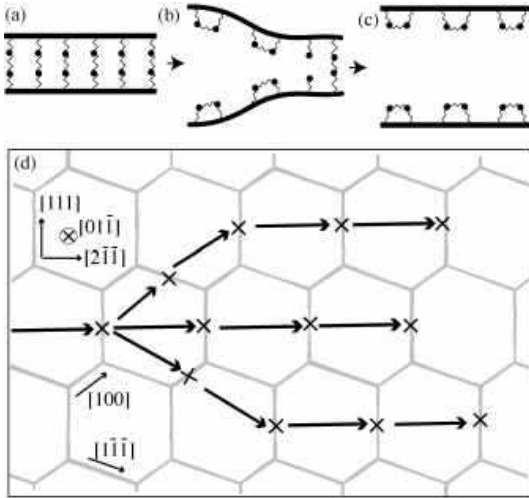


FIG. 1: (a)-(c) : An illustration of cleavage process, in which the surface reconstruction is described schematically as surface dimerization. (d) : Cleavage paths on Si(111) plane with or without step formation. The upper path of step formation is classified into ‘[2 $\bar{1}$ 1]’ or ‘via-(1 $\bar{1}$ 1)-plane’ type, while the lower path is classified into ‘[2 $\bar{1}$ 1]’ or ‘via-(100)-plane’ type (See Section VI, for details).

Now the ‘fast’ process is discussed from a quantum mechanical aspect. Due to the time scale, the reconstruction process in cleavage should occur *locally*. As the most typical process, nearest neighbor dangling bonds tend to form a surface bound state. In other words, the elementary cleavage process should contain *two* successive bond breakings, *not one*; If a *single* bond breaking occurs, the resultant two highly unstable electrons have no counterpart for forming a surface bound state and will recover the initial crystalline bonding. If *two* successive bond breakings occur, the resultant four unstable electrons have counterparts for forming surface bound states, as the surface dimerization in Fig. 1(a)-(c). As discussed later, this nearest neighbor reconstruction mechanism will give directly the experimentally observed (2 \times 1) reconstruction of cleaved Si or Ge (111) surface.

B. Crystalline symmetry

The two essential points are explained, according to the symmetry. The first point comes from the presence of crack tip. In Figs. 1(a)-(c), we find that, during the cleavage process (b), the ‘forward’ (right) and ‘backward’ (left) directions of the cleave propagation are symmetrically inequivalent, due to the presence of the crack tip.

In the initial (a) and final (c) structures, on the other hand, the two directions are equivalent.

The second point comes from the crystalline symmetry of a real solid. Figure 1(d) shows the actual cleavage paths on the Si(111) plane, with or without step formation. Here the cleavage propagation direction is the [2 $\bar{1}$ 1] direction. The system does not have the mirror symmetry with the cleavage plane, unlike the toy model of Figs. 1(a)-(c). In result, the two cleaved surfaces, the upper and lower ones, are symmetrically inequivalent, during the cleavage process. Especially, the upper and lower paths of step formation in Fig. 1(d) are symmetrically inequivalent. The inequivalence of the step formation paths can be found experimentally in resultant cleaved surfaces and will be investigated in this paper.

It should be noted that the two symmetrical inequivalences are different in their origins; The inequivalence of the ‘forward’ and ‘backward’ directions is due to the global shape (crack) of the sample. This inequivalence is present even in a continuum medium picture. The inequivalence of the upper and lower cleaved surfaces, on the other hand, is inherent in the atomic (diamond) structure and is absent in a continuum medium picture.

C. Role of large-scale electronic structure calculation

The above discussions give the essential role of electronic structure calculations, since the atomistic theory for cleavage is required to contain (i) surface reconstruction processes described by electronic structure, and (ii) explicit crack tip that causes the symmetrical difference on system. Several theoretical works^{8,9,14} cover the two requirements but the investigation is still limited. An investigation beyond the limitation is given by the present large-scale simulations with the system sizes on the order of 10 nm. Remarkable results are the direct observations of step formation and bending of cleavage planes, as well as the elementary reconstruction processes.

III. METHODOLOGY OF SIMULATION

A. Large-scale electronic structure calculation

For recent years, we have developed theories and program codes for large-scale electronic structure calculations.^{15,16,17,18,19} Their common mathematical foundation is to calculate the one-body density matrix $\hat{\rho}$, in stead of one-electron eigen states $\{\phi_k^{(\text{eig})}\}$. The density matrix $\hat{\rho}$ is defined, formally, as

$$\hat{\rho} \equiv \sum_k^{\text{occ.}} |\phi_k^{(\text{eig})}\rangle \langle \phi_k^{(\text{eig})}|. \quad (1)$$

Any physical quantity $\langle \hat{X} \rangle$ is described as

$$\langle \hat{X} \rangle \equiv \sum_k^{\text{occ.}} \langle \phi_k^{(\text{eig})} | \hat{X} | \phi_k^{(\text{eig})} \rangle = \text{Tr}[\hat{\rho} \hat{X}]. \quad (2)$$

Among the methods, the present simulations are carried out by the method with generalized Wannier state,^{15,16,17} which is suitable for covalent materials. The pioneering works of the generalized Wannier states were done by Walter Kohn,^{21,22} in the context of large-scale calculations. The generalized Wannier states $\{\phi_i^{(\text{WS})}\}$ are formally defined as the unitary transformation of occupied eigen states $\{\phi_k^{(\text{eig})}\}$:

$$|\phi_i^{(\text{WS})}\rangle = \sum_k^{\text{occ.}} U_{ik} |\phi_k^{(\text{eig})}\rangle, \quad (3)$$

where U_{ik} is a unitary matrix. The sum of the one-electron energies gives the correct band structure energy;

$$E_{\text{bs}} \equiv \sum_k^{\text{occ.}} \langle \phi_k^{(\text{eig})} | H | \phi_k^{(\text{eig})} \rangle = \sum_i^{\text{occ.}} \langle \phi_i^{(\text{WS})} | H | \phi_i^{(\text{WS})} \rangle. \quad (4)$$

In a qualitative picture, the Wannier state is well-defined localized ‘chemical’ wavefunctions in condensed matters, such as a bonding state or a lone-pair state, with a slight spatial extension. The suffix i of the Wannier state $\phi_i^{(\text{WS})}$ denotes its localization center. For simplicity, a Wannier state $\phi_i^{(\text{WS})}$ will be sometimes denoted by ϕ_i , without the indication of (WS). See Appendix B for details.

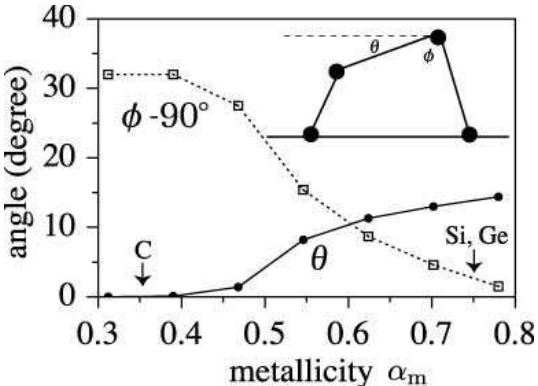


FIG. 2: The dimer geometry on the (001) surface of the group IV elements (C, Si and Ge). The tilt angle θ and the angle ϕ are plotted. The angle ϕ is defined as the one between the surface dimer and the plane that contains the two back bonds of the upper atom. The electron system is described under the energy scaling theory with the metallicity α_m .

B. Transferable Hamiltonian and universality of electronic structure

Another foundation for large-scale calculation is to use the transferable Hamiltonian in the Slater-Koster (tight-

binding) form, which can describe several different circumstances, *e.g.* crystalline phases, liquid, amorphous, defects and surfaces. In the present paper, we use the form in Ref.²³, a typical one, except where indicated. The success of these Hamiltonians is based on the universality of electronic structure, known for decades^{24,25,26}. The universality can be founded by the *ab initio* theory.^{27,28,29}

Now we focus the group IV elements. As the consequence of the universality, the electronic structure of these materials can be systematically described by a one-parameter energy scaling theory.^{24,25} The scaling parameter, ‘metallicity’ α_m , is defined for a given Hamiltonian of the minimal (*s* and *p*) bases as

$$\alpha_m \equiv \frac{\varepsilon_p - \varepsilon_s}{2t_{sp^3}}. \quad (5)$$

Here the numerator ($\varepsilon_p - \varepsilon_s$) is the energy difference between the atomic *s* and *p* orbitals, or the band center difference between the *s* and *p* bands. The parameter t_{sp^3} is the transfer energy along a bulk (sp^3) bond ($t_{sp^3} \equiv |V_{ss\sigma} - 2\sqrt{3}V_{sp\sigma} - 3V_{pp\sigma}|/4$). In general, the energy scaling by transfer energy is directly related to the length scaling by lattice constant. Therefore, the one-parameter theory means that the electronic structure is universal in the scaled energy or length scale. Typical values for the elements are $\alpha_m = 0.35$ for C³⁰ and $\alpha_m = 0.75 - 0.78$ for Si and Ge.³¹ The values of the metallicity α_m for Si and Ge are almost indistinguishable, due to the similarity of the electronic structures (of the valence band) in Si and Ge.³²

Several differences in surface structures among C, Si and Ge are explained by the energy scaling theory. An example is the geometry of the surface dimer on (001) surfaces. The asymmetric dimer for Si(001) was predicted in 1979,³³ before it was established from experiments. Nowadays the standard *ab initio* calculation shows that a *symmetric* dimer appears in the C case and quite similar *asymmetric* dimers appear in the Si and Ge cases. See Fig.2 of Ref.³⁴, for example. Figure 2 shows that the above trend is reproduced with the present Hamiltonian by tuning the value of α_m , which is carried out by tuning the value of $(\varepsilon_p - \varepsilon_s)$. Here we point out that the (111)-(2 \times 1) cleaved surface is also commonly seen in Si and Ge³⁵. From above discussion, the cleavage process of Si and Ge can be expected to hold a common mechanism by the present Hamiltonian.

C. Cleavage simulation and surface energy

The outline of the present cleavage simulations is explained. The simulations will be carried out mainly with the sample size on the order of 10 nm. As explained in Appendix A, the cleavage simulation requires a *strong* external load whose physical origin is the concentrated elastic field in a macroscale (experimental) sample. We carry out the simulations with different ways of imposing external load and find the intrinsic natures of cleavage.

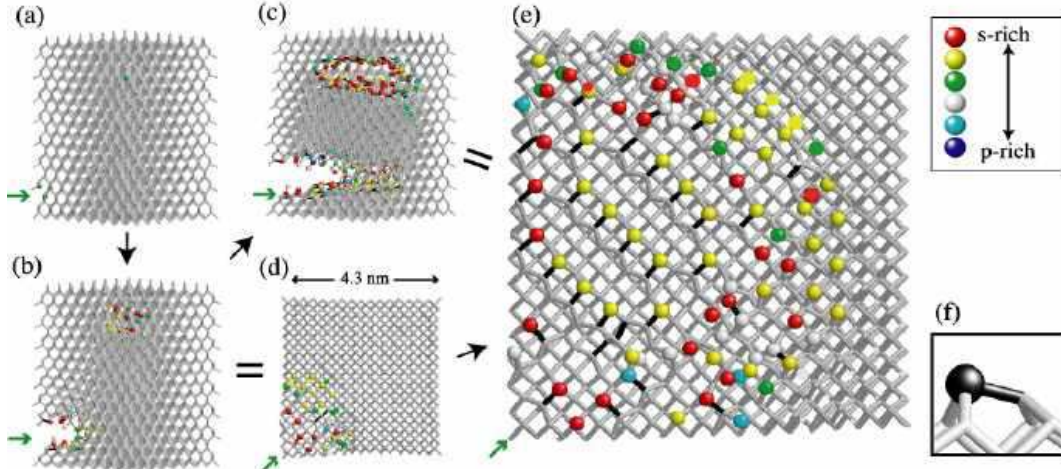


FIG. 3: Cleavage process of a silicon nanocrystal under [001] external load. (a)-(c):The 3D views of successive snapshots with the time interval of about 0.7 ps. (d)(e):Top views of the lower cleavage plane, a (001) surface, in the snapshot (b) and (c), respectively. The green arrow is a viewpoint. (f) Example of the asymmetric dimer geometry. Rods and balls are drawn by the spatial extension of wavefunctions; A rod indicates a bonding state and a ball indicates a atomic (non-bonding) state almost localized on an atom site. For the atomic states (balls), the color corresponds to the weight of the s orbitals ($f_s^{(i)}$); (i) $0 \leq f_s^{(i)} \leq 0.2$ for blue, (ii) $0.2 \leq f_s^{(i)} \leq 0.3$ for cyan, (iii) $0.3 \leq f_s^{(i)} \leq 0.4$ for white, (iv) $0.4 \leq f_s^{(i)} \leq 0.5$ for green, (v) $0.5 \leq f_s^{(i)} \leq 0.6$ for yellow and (vi) $0.6 \leq f_s^{(i)}$ for red. Note that, in larger samples, the (001) cleavage mode will be fairly unstable, due to step formations.¹⁷

Several surface energies are calculated with the present Hamiltonian, so as to confirm the quantitative accuracy. The calculated values are listed below with those by *ab initio* calculations¹¹ inside the parentheses; $\gamma_{001}^{4 \times 2} = 1.58$ (1.41) J/m², $\gamma_{111}^{2 \times 1} = 1.97$ (1.44) J/m² and $\gamma_{110}^{\text{buckled}} = 2.11$ (1.70) J/m², for the (001)-c(4 \times 2) structure, the π -bonded (111)-(2 \times 1) structure and the buckled (110) structure, respectively.³⁶ We find that the present Hamiltonian reproduces the *ab initio* results satisfactory, especially, the order of magnitude ($\gamma_{001}^{4 \times 2} < \gamma_{111}^{2 \times 1} < \gamma_{110}^{\text{buckled}}$), though the absolute values are somewhat overestimated. The present Hamiltonian was also used to several reconstructed (001) surfaces,³⁷ which gives satisfactory results too.

IV. LIMITED STABILITY OF (001) CLEAVAGE

A. Formation of surface dimer

Since experiments reported only the (111) or (110) cleavage plane, the theory should explain why other surfaces *do not* appear. Here we focus the possibility of (001) cleavage plane, because the surface energy of the reconstructed (001) surface is smaller than that of the (111)-(2 \times 1) surface ($\gamma_{(001)}^{4 \times 2} < \gamma_{(111)}^{2 \times 1}$). This means that the absence of (001) cleavage surface can not be explained by the simple prediction from surface energy and is worth investing.³⁸

The possibility of (001) cleavage plane is investigated

in our previous work,¹⁷ in which the (001) cleavage planes are observed within small sample sizes, less than 10 nm. With larger sizes, the flat (001) cleavage surface becomes fairly unstable and forms steps, so as to release the anisotropic surface strain energy. Such strain relaxation mechanism is absent in smaller samples, because a small sample does not contain enough number of atoms that accumulate the strain energy. These observations imply that the cleavage behaviors of nanoscale and macroscale samples can be different and the crossover on the length scale is expected. The presence of the crossover is consistent to the continuum mechanics of cleavage or brittle fracture (See Appendix A). The energy competition between strain relaxation and step formation is also reported in the step structure on equilibrium Si(001) surfaces,^{39,40} in which the crossover is found in the misoriented angle from the ideal (001) plane. Since the calculated surface energy does not contain the possibility of forming steps or accumulating strain energy, these discussions show the importance of large-scale calculations.

Figures 3(a)-(c) show a cleavage process with forming a (001) cleavage surface. The sample is a cubic one with the edge length of about 4 nm and contains 4501 atoms. The simulation is carried out with the external load in the [001] direction. See Appendix C for details. In result, the cleavage starts from two points on the sample edges and two cleavage planes appear. The lower cleavage surface is shown in Figs. 3(d) and (e). Figure 3(e) contains the asymmetric dimers whose geometry is shown

in Fig. 3(f). The formation of the dimer was already discussed in Fig. 2. As a remarkable result, a well-defined dimer row domain can be found in Fig. 3(e), as usual on an equilibrium Si(001) surface.⁴

In Fig. 3, a rod or ball is assigned for each wavefunction (Wannier state), according to the weight distribution among atoms (See Appendix B for Wannier states). A rod is assigned for a bonding orbital, localized at a pair of atoms. The black rods are the reconstructed bonds that are not seen in the initial (crystalline) structure. One should note that a bond is defined by the calculated wavefunctions, not by an atom pair distance. A ball is assigned for an atomic (non-bonding) orbital, localized on an atom site. No ball appears in the initial crystal, since all the wavefunction forms the bulk bonding states. After a bulk bond is broken, the corresponding wavefunction is stabilized with increasing the weight of *s* orbitals. This energy gain mechanism is called ‘dehybridization’,²⁴ since the *sp*³ hybridization is cancelled. For quantitative discussion of the dehybridization mechanism, a parameter $f_s^{(i)}$ is defined,¹⁷ for a wave function ϕ_i , as

$$f_s^{(i)} \equiv \sum_I |\langle \phi_i | I s \rangle|^2, \quad (6)$$

where $|I s\rangle$ is the *s* orbital at the *I*-th atom. For example, $f_s^{(i)} = 1/4$ in an ideal *sp*³ hybridized state. The dehybridization mechanism is clearly seen, as the drastic change of $f_s^{(i)}$.¹⁷ To visualize the dehybridization mechanism, the atomic (non-bonding) states are classified by the color of ball, according to the value of $f_s^{(i)}$ (See the caption of Fig. 3). Red or yellow balls, *s* rich states ($f_s^{(i)} \geq 0.5$), are seen mainly on cleaved surface, due to the dehybridization mechanism. In cleaved surface, the asymmetric dimer has a ball on the upper atom, as in Fig. 3(f), which indicates a doubly occupied surface states that are localized on the atom. In other words, the upper atom of the dimer has an excess electron population and the lower one has a deficit population, as usual on Si surfaces.⁴¹

B. Anisotropic surface strain due to crack tip

The tilting freedom of the surface dimer can be influenced by the anisotropic surface strain due to the crack tip. To clarify the discussion, we carried out another calculation, in which the periodic boundary condition is imposed, by eight atomic layers, in the $[\bar{1}10]$ direction. Figure 4 shows the result of a subsystem or a ‘slice’ that contains atoms only within two atomic layers, the minimum crystalline periodicity, in $[\bar{1}10]$ direction. Note that the drawing manner is changed from that in Fig. 3; Bonds (rods) are drawn just for an eye guide. The excess or deficit electron population is marked as the sign ‘+’ or ‘-’, respectively, in stead of the presence or absence of a ball. The present drawing manner will be used hereafter

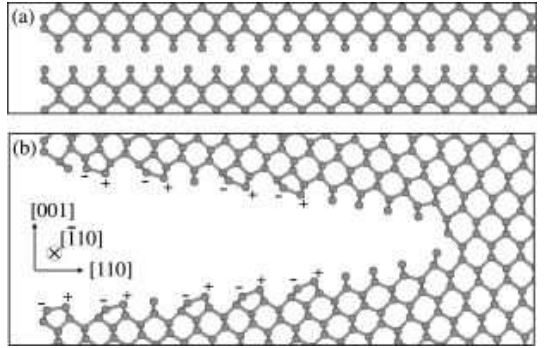


FIG. 4: Cleavage process on (001) plane; (a) Ideal geometry with a parallel separation (b) A snapshot during the simulation. The figure shows a subsystem or a ‘slice’ that contains atoms within two layers in the $[\bar{1}10]$ direction. Bonds (rods) are drawn just for an eye guide. The mark ‘+’ or ‘-’ on atom indicates the excess or deficit electron population, respectively. Note that a non-dimerized surface atom has a (doubly occupied) lone pair state.¹⁷

in this paper. The reason of changing the drawing manner will be explained, in Section V, with the quantum mechanical analysis of cleaved (111) surfaces.

When the tilting direction for a surface dimer is defined as the vector from the lower atom into the upper one, all the dimers of Fig. 4(b) shows the same tilting direction as the cleavage propagation direction. The same tendency is seen in the dimer row domain of Fig. 3(e). In the flat (001) surface, however, the alternately tilted structure, called $c(4 \times 2)$ structure, is more energetically favorable by about 0.1 eV per a dimer pair.¹¹ In other words, the observation of the unique tilting direction among the surface dimers can not be explained by surface energy.

The tendency is understood by the fact that the presence of the crack tip causes the symmetrical inequivalence between the ‘forward’ and ‘backward’ directions of cleavage propagation, as in Fig. 1(b). In the ideal geometry (Fig. 4(a)), the forward (right) and backward (left) directions are symmetrically equivalent. On the cleaved surfaces (Fig. 4(b)), however, the two directions are no more equivalent and an anisotropic surface strain is imposed on the surface dimers.

To end up this section, we repeat that the well-defined (001) surface appears *only among smaller samples*. This point will be discussed again, in Section VII, as bending of the cleavage plane from (001) plane into (111) plane. It should be also noted that the (001) or (100) surface appears as the step edge in a step formation process (See Section VI C).

V. (2 × 1) STRUCTURE IN (111) CLEAVAGE PROCESS

We turn to discuss the (111) cleavage plane, known as the most favorable one. The π -bonded structure,

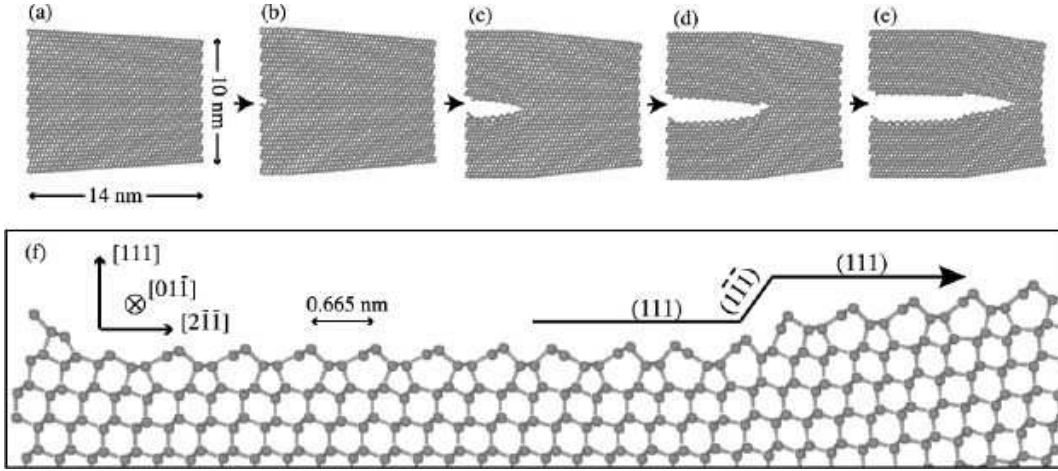


FIG. 5: Cleavage process of silicon with the (111)-(2 \times 1) cleaved surface. (a)-(e): Successive snapshots with the time interval of about 2 ps. (f): A part of the lower cleavage surface in the snapshot (e). A step is found and is classified into the ' $\bar{[211]}$ -type' or 'via-($\bar{1}\bar{1}\bar{1}$)-plane type' that can be decomposed into the successive bendings of cleavage planes as (111) \rightarrow ($\bar{1}\bar{1}\bar{1}$) \rightarrow (111).

proposed by Pandey,⁵ is widely accepted as the atomic structure of the cleaved (111)-(2 \times 1) surface of Si and Ge.^{4,6,7,8,9,10,35} We focus the cleavage mode with the [211] propagation directions (See Fig. 1(d) for geometry), because the situation is consistent to typical experiments (See Fig. 1 of Ref. ⁴², for example). The simulations in this section are carried out with the external load in the [111] direction. See Appendix C for details. The periodic boundary condition is imposed in the [011] direction, which is orthogonal to the cleavage propagation direction. The periodic length contains eight atomic layers or is four times larger than that of the minimum crystalline periodicity. For a systematic investigation, first we impose the '2D-like' constraint, the constraint on atomic motion by the minimum crystalline periodicity in the [011] direction. Later, in Section VI C, we will release the constraint.

Figure 5 shows an example of the simulation result where a step appears. The sample contains 11,096 atoms. The bonds (rods) are drawn just for an eye guide in Fig. 5(f) and similar figures hereafter. From Fig. 5, the cleavage propagation velocity is estimated to be $v_{\text{prop}} \approx 2 \text{ nm/ps} = 2 \text{ km/s}$, which is on the order of, but less than, the Rayleigh wave velocity ($v_R = 4.5 \text{ km/s}$), as discussed in Section II A. The cleaved surface in Fig. 5(f) contains the π -bonded (111)-(2 \times 1) structure, of which unit structure is a set of seven- and five-membered rings. The quantum mechanical analysis will be done in Section V A. The observed step will be discussed in Section VI.

A. Elementary reconstruction process

Figures 6(a)-(e) shows an example of forming the (2 \times 1) reconstruction. The appearance of the (2 \times 1) structure is shown schematically in Figs. 6(f)-(g), which

is explained semi-qualitatively as follows: With two successive bond breakings in the [211] direction, a (2 \times 1) structure appears in the snapshot of Fig. 6(b), which is schematically shown in Fig. 6(e). This (2 \times 1) structure is identical to the proposed one in Ref.⁴³ and is called 'buckled (2 \times 1) structure' in this paper. The buckled structure is formed, when the two dangling-bond electrons of the C and D atom sites are transformed into a lone pair state at the D atom site. In Fig. 6(e), the oval at the D atom site indicates the presence of the lone pair state. As the general quantum mechanical tendency,⁴¹ the D atom site with the excess electron population moves into the upper (vacuum side) region, while the C atom site with the deficit electron population moves into the lower (bulk side) region. Then, the buckled structure is transformed into the π -bonded structure, in Fig. 6(d), which is schematically shown in Fig. 6(f). The transformation is completed by the two successive changes of wavefunctions; (i) The atomic (lone pair) state at the D atom site is transformed into the π -bonding state between the B and D atom sites. In the three-dimensional view, a π -bonding zigzag chain appears in the perpendicular direction to the page. (ii) The bond between the A and B atom sites is transformed into one between the A and C sites. In the final structure, Fig. 6(f), the B or D atom site has three electrons in σ bondings and one electron that belongs to the π -bonding zigzag chain. All the other atoms are in the four coordination number in σ bondings. Hereafter, the transition from the buckled structure into the π -bonded one is called 'BP transition'.

The actual π -bonded structure shows a tilting among the B and D atom sites. The structure in Fig. 6(f) is one of the two possible tilted structures, in which the D atom site is placed at the upper side. In the other tilted structure, the B atom site is placed at the upper side. Both structures are seen in Fig. 5. In the BP transition

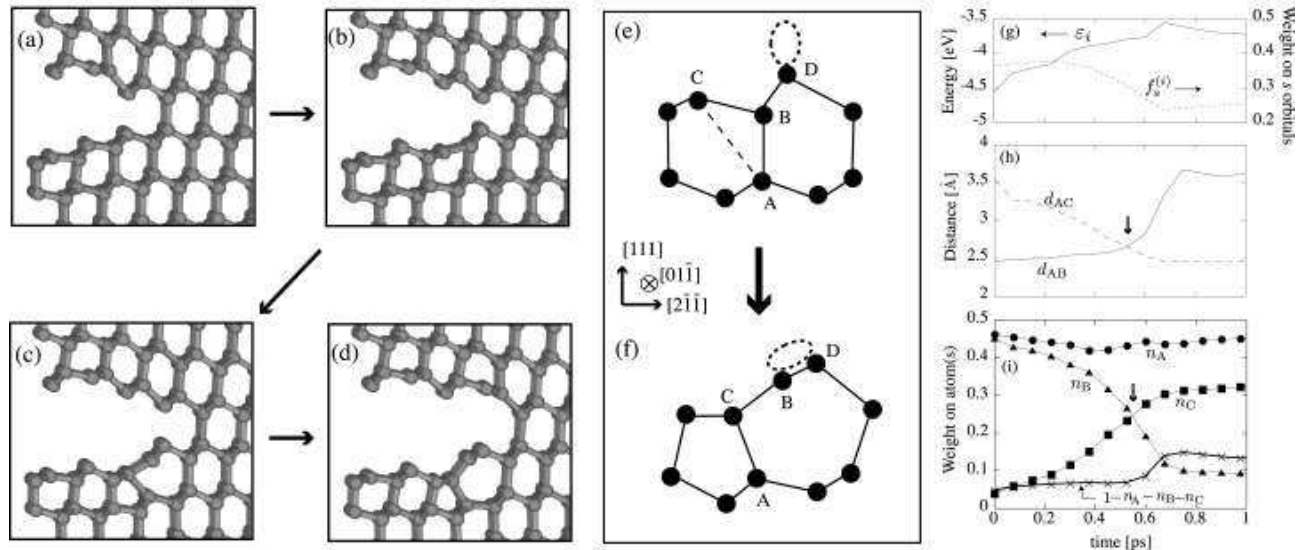


FIG. 6: (a)-(d):Initiation of cleavage with forming the (111)-(2x1) structure. (e)-(f): Schematic figures of the transition from (e) the buckled (2x1) structure into (f) a (tilted) π -bonded (2x1) structure. The former structure appears on the lower cleaved surface in (b) and the latter appears in (e). The oval in (b) indicates the presence of a lone pair state on the D atom site. The oval in (c) indicates the π -bonding zigzag chain in the direction perpendicular to the page. (g)-(i): Quantum mechanical analysis of a BP transition in which the bonding wavefunction (ϕ_i) between A and B atom sites turns to that between A and C atom sites; (g) The one-electron energy $\varepsilon_i \equiv \langle \phi_i | H | \phi_i \rangle$ and the weight of s orbitals $f_s^{(i)}$ for the wavefunction ϕ_i . (h) The atomic distance between A and B atom sites (d_{AB}) and that between A and C atom sites (d_{AC}). (i) The weight distributions of the wavefunction ϕ_i on the A, B and C atom sites (n_A, n_B, n_C). The rest of the weight ($1 - n_A - n_B - n_C$) is also plotted.

process, the tilted structure appears, at first, with the D atom site as the upper one, like Fig. 6(f), since the D atom belongs to a higher layer than the B atom site in the initial geometry. The standard *ab initio* calculations give a small difference in the surface energy, about 0.01 eV per (2x1) cell,¹¹ between the two tilted structure. In this paper, we do *not* focus our consideration to the difference between the two tilted structures and call them, commonly, π -bonded structure.⁴⁴ We focus, instead, the common property of the tilted structures, that is, the fact that the upper atom always has an excess electron population, due to the general quantum mechanical feature.⁴¹ Several *ab initio* calculations, such as Fig. 2 of Ref.¹⁰, give the corresponding occupied surface state localized on the upper atom.

Now the BP transition is analyzed quantum mechanically by monitoring the appearance of the seven- and five-membered rings. In Figs. 6(e)-(f), we focus the wavefunction ϕ_i that is localized between the A and B atom sites at the initial structure. Several quantities are plotted as the functions of time; Figure 6(g) shows the one-electron energy $\varepsilon_i \equiv \langle \phi_i | H | \phi_i \rangle$ and the weight of s orbitals $f_s^{(i)}$, defined by Eq.(6). These quantities were monitored in the reconstruction process on the (001) surface (See our previous work¹⁷). Figure 6(h) shows the atomic distances d_{AB} and d_{AC} , between the A and B sites and between the A and C sites, respectively. Figure 6(i) shows the weight distributions of the wavefunction ϕ_i on

the A, B and C atom sites (n_A, n_B, n_C). The rest of the weight ($1 - n_A - n_B - n_C$) is also plotted. The initial wavefunction is a bonding state, whose dominant weight is localized on the A and B atom sites ($n_A + n_B \approx 0.9$). The final wavefunction is a bonding state that is localized on the A and C atom sites ($n_A + n_C \approx 0.8$). The behavior of the atomic distances (d_{AB}, d_{AC}) is consistent to the above picture of the change from the B-A bonding state into the A-C bonding state.

The intermediate wavefunction of the transition process is discussed. The bold arrows in Figs. 6(h) and (i) indicate the time of $d_{AB} = d_{AC}$ and $n_B = n_C$, respectively. The two arrows indicate almost the same time, when the wavefunction is an intermediate state between the B-A and A-C bonding states and shows a spatial extension over the three atom sites (B-A-C). The intermediate wavefunction shows no characteristic feature, such as maximum, minimum, plateau or discontinuity, in the energy ε_i and the hybridization freedom $f_s^{(i)}$. We should recall that the wavefunction on (001) surface shows a two-stage reconstruction process¹⁷, in which a metastable atomic state appears with a large weight on s orbital ($f_s^{(i)} \approx 0.8$). In the present case, on the other hand, the intermediate state is not metastable and the process is not a multi-stage one. Note that, in Fig. 3, we classified the wavefunctions into an atomic state or a bonding state. The intermediate state seen in Figs. 6(g)-

(i) can not be classified into these categories, because of the spatial extension over the two bond sites ($B-A-C$).

It should be emphasized that the mechanism of forming the (2×1) structure in Fig. 6(e) is reduced to the simple picture in Section II A, because *nearest neighbor* dangling-bond electrons form a surface bound state.

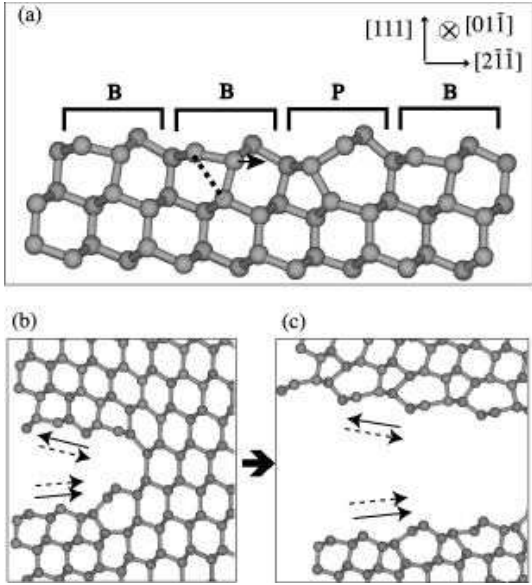


FIG. 7: (a) Surface calculation with a coexistence of the buckled and π -bonded (2×1) structures. An induced strain is shown as an arrow at the boundary between the buckled and π -bonded structures. The dashed line indicates the bond site that will appear after the induced next BP transition. (b)-(c): Two snapshots in a cleavage process. The arrows indicate the direction of the two possible anisotropic strains; The solid arrow corresponds to the direction of the strain field due to the BP transition, which is shown in (a). The dashed arrow corresponds to the strain due to the global (crack opening) geometry. In the snapshot (c), a constant force is imposed in the left direction on several left most atoms of the upper cleaved surface, as a boundary condition of surface strain (See text).

B. Competition of anisotropic surface strains

Now we discuss why the π -bonded structure appears on the lower cleavage surface in Fig. 6(d), but not on the upper one. The fact is explained by the competition of two surface strains; One rises from the global (crack) shape, which can cause an anisotropic surface strain in the cleavage propagation direction. This strain mechanism is *not* inherent in crystalline structure and can appear even in a toy model of Fig. 1(b). We have discussed, in Section IV B, that this strain mechanism plays a crucial role on the (001) surface.

Another strain mechanism rises from the atomic structure of the reconstructed (111) surface. As a demonstration, Fig. 7(a) shows a calculated (111) surface with the

coexistence of the buckled and π -bonded (2×1) structures. The periodic boundary condition is used in the $[01\bar{1}]$ direction and all the sample surfaces are terminated (See Appendix C) except the upper one. Now we find that the π -bonded structure induces an anisotropic strain force shown as an arrow. The strain force enhances a further BP transition of the next left unit by increasing the atomic distance d_{AB} of Figs. 6(e)-(f) and decreasing d_{AC} .

The directions of the two surface strains are drawn as arrows in an actual cleavage process of Fig. 7(b). The dashed arrows indicate the strain force due to the global (crack) shape. The direction of the force lies in the ‘forward’ direction of cleavage propagation both on the upper and lower surfaces. The solid arrows indicate the strain force for enhancing the BP transition. Due to the crystalline symmetry, the force lies in the opposite directions on the upper and lower surfaces. On the lower surface, the two strain forces are in the same direction, which enhances the successive BP transition. On the upper surface, on the other hand, the two strain forces are in the opposite direction, which suppresses the successive BP transition. This situation explains why the BP transition appears only on the lower cleaved surface in Fig. 7(b). It is essential that the inequivalence between the upper and lower cleavage surfaces is caused by the symmetry of the (111) surface. Here we recall the fact that the ‘forward’ (right) and ‘backward’ (left) directions of cleavage propagation are equivalent in Fig. 4(a), the ideal (001) surface, but are not in Fig. 1(d), the ideal (111) surface.

The above explanation is completed in Fig. 7(c), in which an additional constant force is imposed in the left direction on several left most atoms of the upper cleaved surface. The additional force corresponds to the boundary condition of surface strain, since the simulation sample should be *embedded* in a macroscale sample. In the embedded situation, the boundary region of the simulation sample should be connected with successive π -bonded (2×1) structures and should be under the resultant strain force. In Fig. 7(c), the resultant sample contains the π -bonded (2×1) structures on the upper and lower surfaces. Since the investigations on already cleaved samples support the π -bonded structure,^{6,10} we conclude that the π -bonded structure should appear commonly on the upper and lower surfaces, as in Fig. 7(c).

The present discussion is based on the symmetry of the two strain forces and a quantitative discussion is desirable. We carry out the simulations with various conditions and find that the easiness of the BP transition is dependent on many factors, as well as the strain force at the sample boundary. For example, the BP transition seems to occur easier in a *thicker* sample, with a larger sample length in the $[111]$ direction, since the BP transition accompanies the deformation in deeper layers. A more systematic investigation should be done in future.

The symmetrical inequivalence between the upper and lower cleavage surfaces is clarified, when the present results are compared to previous theoretical works for form-

ing the π -bonded (2×1) structure; By the standard *ab initio* molecular dynamics simulation, a slab system was simulated under a periodic simulation cell,⁷ in which the initial structure was chosen as the ideal surface with small random displacements. Since the paper discussed only single surface, there is no room to consider the inequivalence between the upper and lower surfaces. In a later work,⁸ a slab system was simulated with an internal *parallelly separated* gap. The paper reported the π -bonded (2×1) structures both on the upper and lower cleavage surfaces with a critical gap for the parallel separation (See Figs.1 and 2 of Ref.⁸). The paper also reported that the buckled (2×1) structure was found as a precursor for the π bonded structure, as discussed in Figs. 6(e)-(f). The simulation in Ref.⁸ and the present one lead to the same final structure of the π -bonded (111) - (2×1) structure. The difference rises, however, in the cleavage process, due to the difference of the boundary condition. In Ref.⁸, the actual cleavage simulations with forming the π -bonded (2×1) structure were carried out under the minimum periodicity in the $[2\bar{1}\bar{1}]$ direction. Such simulations do not contain the present competitive mechanism of the two surface strains or the resultant symmetrical inequivalence between the upper and lower surfaces.

VI. STEP FORMATION IN (111) CLEAVAGE PROCESS

A. Classification of steps

Several (111) cleavage simulations contain step formation. For step formation with the gap of two atom layers, there are two symmetrically inequivalent paths; the upper and lower paths in Fig. 1(d). The upper path is called ‘ $[\bar{2}11]$ type’, since the step is descending in the $[\bar{2}11]$ direction. In the same manner, the lower path is called ‘ $[2\bar{1}\bar{1}]$ type’. For example, the step formation in Fig. 5 is classified into the former type (See Section VI B for detailed analysis). Among our simulations, the two types of step are observed.

The two types of step are experimentally reported. Earlier papers^{4,12,45} reported that the *lower* path in Fig. 1(d), the ‘ $[\bar{2}11]$ type’ is predominant. Later experimental papers⁴⁶, however, reported the *upper* path of step, or the ‘ $[\bar{2}11]$ ’ type step.

B. Step formation within 2D-like constraint

First, we present the simulation results within the ‘2D-like’ constraint, in which the atomic motion in the $[01\bar{1}]$ direction is under the constraint of the minimum periodicity of crystal (See the beginning of Section V). This constraint freezes the reconstruction freedom in the $[01\bar{1}]$ direction. Under the constraint, we frequently observed the step formation shown in Fig. 8, which is geometrically equivalent to that in Fig. 5. The dashed lines indicate

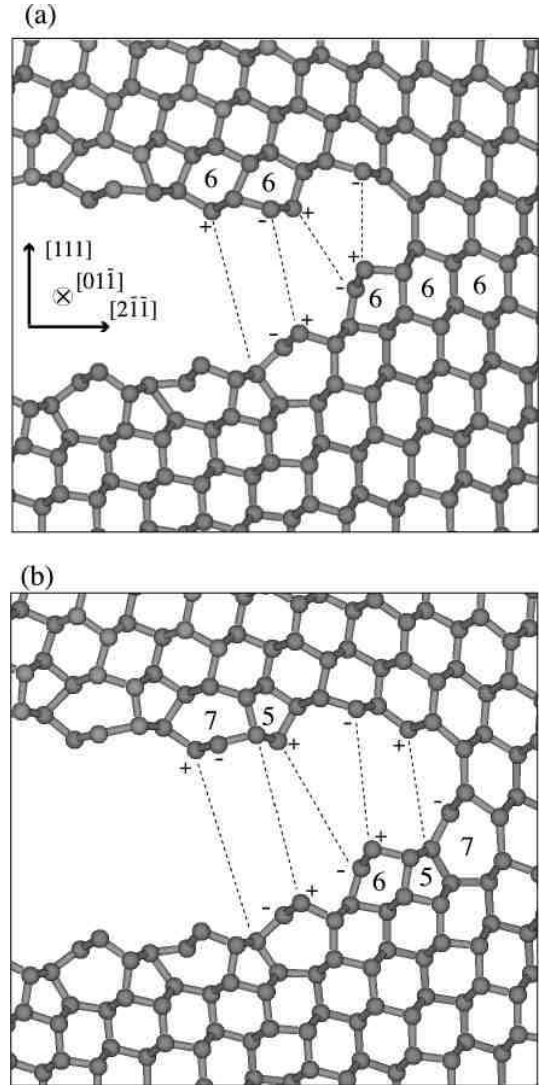


FIG. 8: A step formation process on the (111) cleavage plane. The step is classified into the ‘ $[\bar{2}11]$ ’ or ‘via- $(1\bar{1}\bar{1})$ -plane’ type step (See Fig. 5(f)). Two snapshots with the time interval of about 0.6 ps are shown. The dashed lines indicate the bond sites in the crystalline geometry. The mark ‘+’ or ‘-’ on atom indicates the excess or deficit electron population, respectively. The simulation is carried out with the ‘2D-like’ constraint or the minimum periodicity in the $[01\bar{1}]$ direction.

the bond sites in the crystalline geometry. The observed step is classified into the ‘ $[\bar{2}11]$ type’ or the upper path of Fig. 1(d). The members of several rings are plotted, as ‘6’, ‘5’ or ‘7’, so as to clarify the reconstruction. An important point is that the resultant upper and lower surfaces are symmetrically inequivalent. The step edge of the lower surface is a six-membered ring, marked ‘6’, while that of the upper surface is a five-membered ring, marked ‘5’. We recall that the inequivalence between the upper and lower surfaces was discussed, without step formation, in Section V B.

The mechanism of the step formation is discussed.

This step can be decomposed into the successive bendings in cleavage path as $(111) \rightarrow (1\bar{1}\bar{1}) \rightarrow (111)$ planes (See Fig. 1(d) and Fig. 5). In other words, the step is formed *through* the $(1\bar{1}\bar{1})$ plane and we call the step ‘via- $(1\bar{1}\bar{1})$ -plane’ type. First, we ignore the reconstruction (or quantum mechanical) freedom and try to give a simple explanation; In the continuum mechanics with a macroscale picture, the divergent elastic field is the motive force for cleavage (See Appendix A). In the crystalline geometry, on the other hand, the (111) and $(1\bar{1}\bar{1})$ planes are symmetrically equivalent. These facts explain the easiness of the step formation, since the bendings between equivalent planes can be formed by the fluctuation of elastic field, especially in its angular dependence.

Even when the reconstruction freedom is considered, the easiness of this step formation is found in the stability mechanism of the surface states; Since these surface states cause an excess or deficit electron population on atom, we analyzed the electron population among surface atoms, as in the Si(001) case in Fig. 4. An atom marked with ‘+’ or ‘-’ means one with an excess or deficit electron population, respectively. An initial bonding state, indicated as a dashed line in Fig. 8, is changed into a surface bound state mainly localized on a ‘+’ atom site. The stability of the structure is understood by the fact that the number of broken bonds (dashed lines) is identical to that of the surface bound states (‘+’ atom sites) and there is no unstable dangling bond electron. In addition, we find the following features: (i) The ‘+’ and the ‘-’ sites appear in the alternate alignment, which means an energetical balancing. (ii) A ‘+’ site is always placed at the vacuum side of a buckled structure, while a ‘-’ site is placed at the bulk side. (iii) The values of the excess or deficit population are, typically, on the order of $0.1 e$. These features are based on the general quantum mechanical tendency⁴¹ and are commonly observed on the flat (non-stepped) (111) surface (See Section V A) and on the (001) surface (Fig. 4).

From the above quantum mechanical analysis, the present step structure is concluded to be a possible one, though it has not yet be confirmed by experiments. It should be noted that we do *not* conclude the present type step as the *most favorite* one, since the present simulation is done under the 2D-like constraint. This point will be taken up at the last paragraph in the next subsection.

Now we comment on a pioneering theoretical paper in 1981,⁴⁷ in which the two step types, the upper and lower path in Fig. 1(d), are compared under several assumptions of atomic structures. In the paper,⁴⁷ the easiness of the *lower* path was supported by an energy gain mechanism, but *not* the *upper* path, which seems to be in contrast to the present result of forming the *upper* path. The contrast comes from the fact that the present step structure is different, in reconstruction, from that assumed in Ref.⁴⁷ The essential point for step formation is how the dangling bond electrons at the step edge are rebonded with reconstruction. In the paper,⁴⁷ the dangling bonds at the step edge are assumed to be rebonded

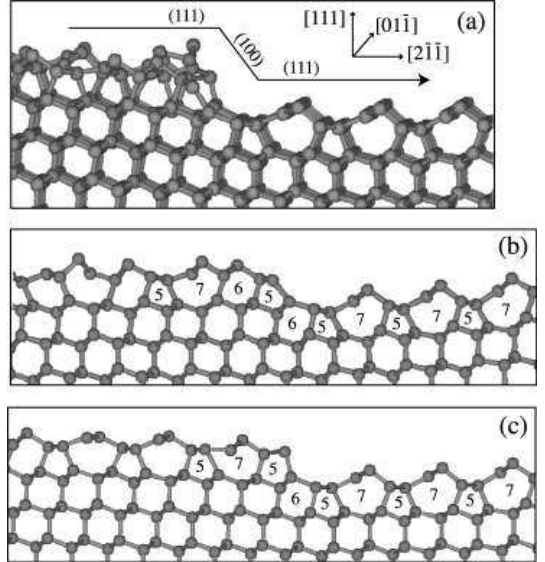


FIG. 9: (a) A stepped area on a (111) cleaved surface. The step is classified into the $[2\bar{1}\bar{1}]$ or ‘via- (100) -plane’ type. (See Fig. 1(d) for geometry). An arrow indicates the cleavage propagation direction. (b)(c): Two ‘slices’ or subsystems of (a) (See text for details).

with each other. In other words, the reconstruction at the step edge was assumed to occur in the $[01\bar{1}]$ direction, *the perpendicular direction* of the page of Fig. 1(d). The paper⁴⁷ reported that such a structure gives only a tiny energy gain and is concluded to be unrealistic. In the present step structure, on the other hand, the dangling bond electrons at the step edge are rebonded *within the plane* of Fig. 1(d), whose stabilization mechanism is explained above.

C. Step formation without 2D like constraint

When we release the 2D-like constraint, the minimum periodicity in the $[01\bar{1}]$ direction, we find the other type of step, the $[2\bar{1}\bar{1}]$ type step or the *lower* path in Fig. 1(d). The result is shown in Fig. 9(a). To observe the freedom in the $[01\bar{1}]$ direction, we classify the atoms, by their initial positions, into four subsystems or ‘slices’. Each ‘slice’ contains atoms within the minimum unit length (two atom layers) in the $[01\bar{1}]$ direction. Four slices are defined in the present simulation and two slices in Fig. 9(a) are shown in Figs. 9(b) and (c).

In Fig. 9(a), the cleaved surface is defective before the step formation. In the defective area of Figs. 9(b) and (c), six membered rings appear in the surface layer, as well as the five or seven membered rings. A defective area also appears in flat (non-stepped) areas, as in Fig. 10. The appearance of the defective six-membered rings means that the reconstruction does not occur by the nearest neighbor dangling bonds *within a slice*. We should recall

the fact that an ideal (111) surface has the symmetry with a $\pm 2\pi/3$ rotation and the (2×1) reconstruction mechanism of Fig.6(e) or (f) is possible in the $[2\bar{1}\bar{1}]$, $[1\bar{2}\bar{1}]$ and $[\bar{1}\bar{1}2]$ directions.

Now we discuss why this type of step does *not* appear within the 2D-like constraint. This type of step formation is decomposed into the successive bendings of cleavage as $(111) \rightarrow (100) \rightarrow (111)$ planes. In other words, the step is formed *through* the (100) plane and we call the step ‘via-(100)-plane’ type (See Fig. 1(d) for geometry). At the step edge, the dangling bond sites is equivalent to those on an ideal (100) or (001) plane. The reconstruction among them is possible with an energy gain of dimerization,⁴⁷ as shown in Fig. 4. Here the $[01\bar{1}]$ direction in Fig.9 is equivalent to the $[110]$ direction in Fig. 4. With the 2D-like constraint, however, the dimerization is prohibited and the step formation of the present type is suppressed, due to the lack of the energy gain mechanism.

From STM experiments, several explicit atomic structures were proposed for this type (the ‘ $[2\bar{1}\bar{1}]$ ’ type) of step.⁴⁵ For comparison with these structures, the atomic structures of the present result are classified, according to the number of the member of rings. We explain the case of Fig. 9(b), for example. Before the step formation, the number of members of the rings are aligned, from left to right, in the order of $5 \rightarrow 7 \rightarrow 6 \rightarrow 5$, in which the last one is the five-membered ring at the step edge. After the step formation, the number of members of the rings are aligned in the order of $6 \rightarrow 5 \rightarrow 7$. We denote the geometry as ‘ $5765/657$ ’, where the slash (/) indicates the step. In the same manner, the geometry of Fig. 9(c) is denoted as ‘ $575/657$ ’. Experimentally proposed structures, Figs. 5(a)-(c) in Ref.⁴⁵ are classified into ‘ $575/6657$ ’, ‘ $765/657$ ’ and ‘ $756/657$ ’, respectively. According to the present classification, the step structure of Fig. 9(b) (‘ $765/657$ ’), is identical to that of Fig.5(b) in Ref.⁴⁵. The structure of Fig.9(c) (‘ $575/657$ ’), is partially identical to that of Fig.5(a) in Ref.⁴⁵ (‘ $575/6657$ ’) in the sense that the geometry of the up stair is identical but that of the down stair is different by one six-membered ring. We should say that the above comparison means only a similarity between the geometries, because the structure of Fig. 9(b) or (c) is that of a slice, not the entire system. We have not yet obtained a ‘ $[2\bar{1}\bar{1}]$ ’ step in which the structure is periodic in the $[01\bar{1}]$ direction *before and after* the step formation.

When we compare the two types of step, the upper and lower paths in Fig. 1(d), the present investigation does *not* determine which should be typical, because the present simulations, even in Fig.9, are carried out under the periodic boundary conditions in the $[01\bar{1}]$ direction. From the discussions in the preceding and present subsections, the appearance of the upper path, the ‘ $[\bar{2}11]$ -type’ step, should be enhanced in the present boundary conditions. We have informed that the two types of step are observed in several STM images⁴⁹ and we consider that a more systematic investigation is desirable both in theory

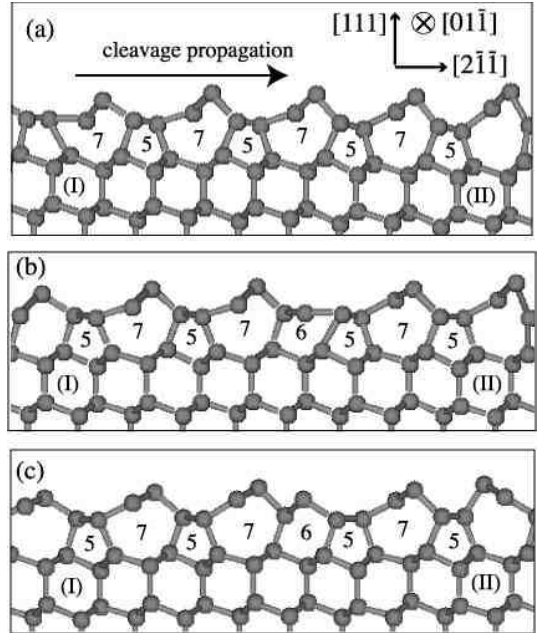


FIG. 10: A defective area on cleaved Si(111) surface. Three slices are picked out. The six-membered rings marked as (I) and (II) are geometrically equivalent among the slices (a)-(c).

and in experiment.

D. Step formation and stability of cleavage mode

The present investigation of step formation implies the stability of the $(111)-(2 \times 1)$ cleavage mode, since a stable cleavage mode on a well-defined atomic plane should be *robust* against possible disorderings and fluctuations. We have discussed that a step formation is decomposed into successive bendings of cleavage plane, such as $(111) \rightarrow (100) \rightarrow (111)$ planes. The former or latter bending process means the deviation or the (quick) recovering of the (111) cleavage mode, respectively. Since the π -bonded (2×1) structure has a π -bonded zig-zag chain in the $[01\bar{1}]$ direction, the direction perpendicular to the cleavage propagation direction, it can accompany the ordering in the $[01\bar{1}]$ direction. Actually, in Fig.9, the step formation changes the cleaved surface from a disordered (defective) structure into an ordered (2×1) structure. The above discussion gives a stability mechanism with a given cleavage propagation direction.

Another stability mechanism can be discussed in the possibility of multiple propagation directions. When the (2×1) structures on the (111) and (001) surfaces are compared, a crucial difference comes from the symmetry. In the limited growth of the (001) cleavage mode, the cleavage propagates easily in the dimerization direction, the $[110]$ direction in Fig. 4.¹⁷ The axis of the dimerization direction is unique for one layer and a (single) step formation changes the axis into the perpendicular direc-

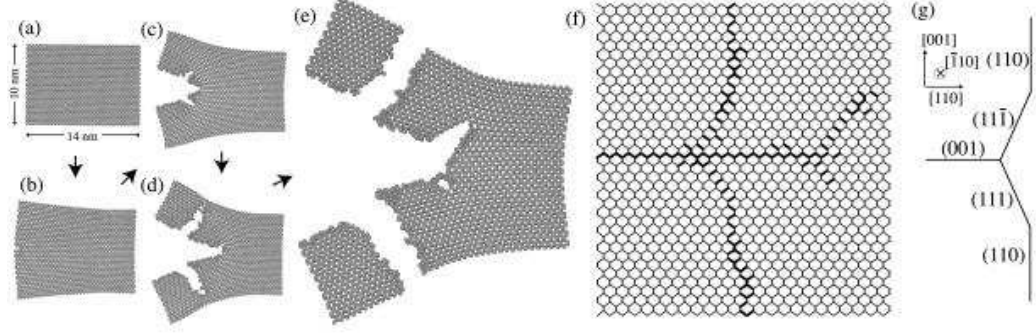


FIG. 11: Cleavage process of silicon with bendings of cleavage planes. (a)-(e): Snap shots with the time interval of about 1 ps. Atoms are drawn as balls from the viewpoint of the $[\bar{1}10]$ direction. (f) : The broken bond sites in the snapshot (e) are plotted as bold lines in the ideal (crystalline) geometry. (g) The indices of the geometry in (f).

tion $((2 \times 1) \rightarrow (1 \times 2))$. Therefore, a cleavage growth with multiple propagation directions requires a step formation and the resultant (001) cleaved surfaces tend to be *rough* with many steps.¹⁷ The (111) surface, on the other hand, has three symmetrically equivalent axes of the easy cleavage propagation; the $[2\bar{1}\bar{1}]$, $[\bar{1}2\bar{1}]$ and $[\bar{1}\bar{1}2]$ axes. For each axis, the π -bonded chain can be formed in the perpendicular direction to the axis. The steps on the (111) surface, unlike on the (001) surface, can preserve the cleavage propagation direction or the direction of the π -bonded chain $((2 \times 1) \rightarrow (2 \times 1))$. In conclusion, the stability of the (111) cleavage mode is implied by the geometrical features; (i) A step can be formed without changing the cleavage propagation direction. (ii) The cleavage propagation direction can be changed without any step formation. We should emphasize that the present stability mechanisms, the robustness against step formation and the possible growth with multiple propagation directions, can not be followed by the conventional discussion with surface energy.

The above feature (ii) should result in multiple domains without any step formation. Actually, a cleaved (111) surface with multiple domains was found in a STM image, Fig.2 in Ref.⁴². We speculate that such a multiple domain structure is formed, because the cleavage propagation directions are locally different. Among the present simulations, however, such a structure can not be observed, due to the periodic boundary condition in the $[01\bar{1}]$ direction.

As discussed in the preceding and present subsections, the present investigation is still limited, due to the artificial periodic boundary condition in one direction. A simulation without any periodic boundary condition should be done in near future with a larger computational resource and/or quantum mechanical methods that have been developed more recently.⁴⁸

VII. BENDING IN CLEAVAGE PATH

Finally, a direct investigation is done for the experimental preference of (111) or (110) surface in cleavage process. We expect that, even if the simulation initiates the cleavage on other planes, the cleavage path will be bent into a more favorable plane. The above statement can be confirmed in simulations. Hereafter symmetrically equivalent planes are called by their ‘type’. For example, $(1\bar{1}\bar{1})$ and $(\bar{1}1\bar{1})$ planes are (111) -type planes.

A cleavage simulation with bendings is shown in Figs. 11(a)-(e). The sample contains 10368 atoms and the sample size is $10\text{nm} \times 14\text{nm}$ on the $(\bar{1}10)$ plane. The periodic boundary is imposed in the $[\bar{1}10]$ direction by eight atomic layers. We prepare an initial ‘seed’ of cleavage on the (001) plane. An external force is acting on the atoms near the sample surfaces except the left one. See Appendix C for details. In short, the external force is given as a two-dimensional central force with a factor K in Eq. (C2) in Appendix C. The continuum mechanics gives a critical value ($K = K_c$) for cleavage. In our simulations, as expected, the cleavage occurs with $K \geq K_c$ and does not occur in a case with $K \approx K_c/10$. Figure 11 is the case with $K \approx 2K_c$.

Figure 11(f) shows the broken bond sites on the crystalline geometry and the corresponding indices are drawn in Fig. 11(g). We find that bendings occur from the initial (001) plane into (111) -type and/or (110) -type planes. An actually observed path shows the bending of $(001) \rightarrow (1\bar{1}\bar{1}) \rightarrow (110)$ planes. The (110) -type planes appear only near the sample surface, which implies that the appearance of (110) -type planes is enhanced by the present sample geometry. Different paths are observed by different simulation conditions, such as tuning the parameter K , preparing a different sample geometry, changing the region of imposing the external force, setting a different cleavage seed, and so on. For example, we observe a bending between two (111) -type planes, such as $(111) \rightarrow (\bar{1}11)$ planes. In the simulations, a (111) -type or

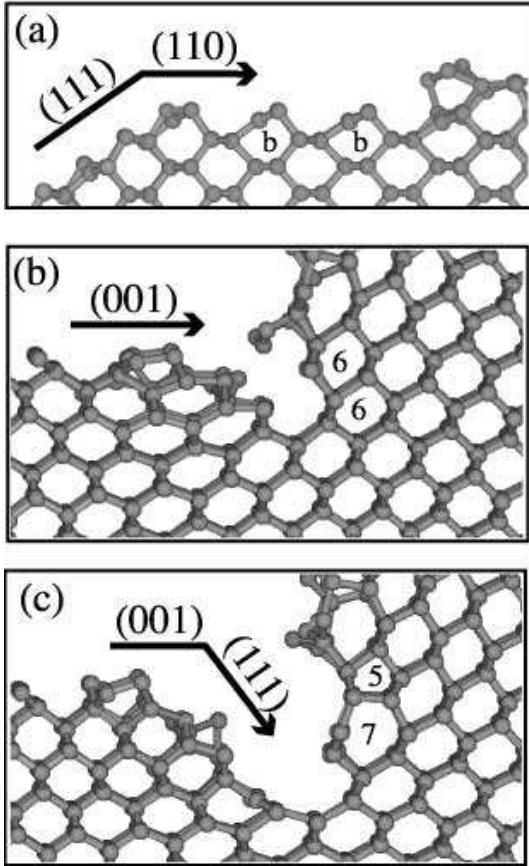


FIG. 12: Appearance of well-defined reconstructed structures after bending in cleavage path. The figures are drawn by projection from the $\langle\bar{1}10\rangle$ direction. The bonds (rods) are drawn just for an eye guide; (a) The bending from (111) plane into (110) plane. After the bending, the buckled structures appear on the (110) plane, which are indicated as ‘b’. (b)-(c) The two snapshots of the bending from (001) plane into (111) plane. The resultant (111) plane contains a (2×1) structure that characterized by the fact that the two six-membered rings, indicated as ‘6’ in (b), are transformed into the seven- and five- membered rings, indicated as ‘7’ and ‘5’ in (c). See Section V for details.

(110)-type plane appears, while no (001)-type plane appears except the initially prepared one. These results are consistent to the experimental preference of the (111)-type and (110)-type cleaved surfaces.

Among the results with bendings, several cleaved areas show well-defined surface reconstructions. In Fig. 12(a), for example, the resultant (110) plane contains the buckled structures, indicated as ‘b’, which is known for a typical reconstruction of (110) plane.¹¹ In the process of Figs. 12(b)-(c), the resultant (111) cleavage plane contains the π -bonded (111)- (2×1) structure. It should be noted that Figs. 12(a)-(c) are projected from the viewpoint of the $\langle\bar{1}10\rangle$ direction and the reconstructed structures reproduce the correct periodicity in the $\langle\bar{1}10\rangle$ direction. In other words, the cleavage propagates from a

disordered or defective surface area into an ordered area.

Though the present result implies the preference of (111) and (110) cleavage planes, the present investigation does not explain the experimental fact that a (110) cleavage plane is less favorable than a (111) plane. A more systematic investigation should be done in future, especially, on the (110) cleavage plane.¹³

VIII. SUMMARY AND DISCUSSION

The present investigation of silicon is summarized as follows: With large-scale electronic structure calculations, the atomistic simulation of cleavage process gives a novel theoretical investigation of cleavage, which can not be reached by the traditional approach with surface energy. The cleavage modes on several different surfaces are compared. Especially, their stability is investigated with the quantum mechanical freedoms of electrons and the anisotropy due to crystalline symmetry. The instability of the (001) cleavage mode (Section IV), an experimentally unobserved mode, gives a general insight in the stability of cleavage. In the (111)- (2×1) cleavage mode, the inequivalence between the upper and lower surfaces are pointed out (Section V), which appears directly in the inequivalence of step formation in the upper and lower directions (Section VI). Several structures for steps are observed and these structures may be important in analyzing experimental STM images. The stability of the (111)- (2×1) cleavage mode is implied by its robustness against step formation and the possible growth with multiple propagation directions. Finally, the predominance of the (111) or (110) cleavage planes, the experimentally observed cleavage planes, are implied by the way of bending of cleavage plane (Section VII). The present results are, still, *not* free from several artifacts, such as finite size effect, way of cleaving (imposing external load), condition of sample boundaries, and the limited quantum mechanical freedoms of electron system. These factors, however, are physically independent and a systematic investigation for each factor can be done in future works.

Apart from the cleavage phenomenon, the present investigation is discussed from the general viewpoints of (I) time scale and (II) length scale. From the viewpoint of time scale (I), the elementary atomistic process is a ‘fast’ surface reconstruction almost free from the thermal equilibration, as discussed in Section II. As a ‘fast’ reconstruction, the rebonding tend to occur between *nearest neighbor* dangling-bond electrons, which directly explains the Si(111)- (2×1) structure on cleaved surface, as discussed in Section V A. Since the local reconstruction mechanism is general in the quantum mechanical picture, we expect the (111)- (2×1) surface also in other processes. Actually, we are informed that the corresponding STM image was found in Si(111) $\sqrt{3} \times \sqrt{3}$ -Ga surface, when the Ga atoms are locally removed at room temperature.⁵⁰ At higher temperatures, the (7×7) structure appears.⁵¹ The

above situation of forming the (2×1) reconstruction is another ‘fast’ process almost free from thermal equilibration. The review article⁴ lists the experimental reports of other processes with appearance of the $(111)-(2 \times 1)$ structure.

From the viewpoint of length scale (II), a crossover is generally expected at the scale of 10 nm. Since the fundamental theory is given by the energy competition between a volume term and a surface term, the general dimensional analysis gives a crossover in length scale. An example is found in the continuum mechanics for cleavage (Appendix A). In the case of silicon, the above energy competition is reduced to that between the sp^3 (bulk) term and the non- sp^3 (surface) term. We speculate that the scale of the crossover is universal, because the surface energy of silicon is always on the same order, 1 J/m²,³⁶ among different indices and reconstructions. As a geometrical discussion of the crossover, a well-defined reconstructed surface appears, only when the system size is much larger than the unit length of the reconstructed surface. In the present investigations of cleavage, the crossover at the scale of 10 nm is found in the instability of the (001) cleavage mode and the formation of step or bending in cleavage path. Another example of the crossover may be seen in the shape of self-organized Si islands;⁵² an island with the size of 10 nm or less has a semispherical shape and an island in larger sizes has a pyramidal shape that has facets with well-defined indices.

The present method of the large-scale electronic structure calculation is widely applicable, not specific for cleavage. In an industrial viewpoint, the structural property with the scale of 10 nm is one of the urgent problem in the present semiconductor technology.⁵³ The expected crossover at the scale of 10 nm is of general importance and can be a future work of the present simulation method.

APPENDIX A: CONTINUUM MECHANICS OF BRITTLE FRACTURE

The continuum mechanics of cleavage or brittle fracture³ should be referred, when the present nanoscale simulations are compared with experiments. A pioneering theory in the continuum mechanics, the Griffith theory,¹ gives the critical crack length c for spontaneous cleavage propagation. The order of the crack length c is given as

$$c \approx \frac{\gamma E}{\sigma^2} \quad (\text{A1})$$

with the external load σ , the Young modulus E , and the surface energy per unit area γ . The essence of the theory is based on a dimensional analysis; Equation (A1) is given by the competition between the energy gain of (three dimensional) strain relaxation and the energy loss of surface formation. The above competition is that between a volume energy term and a surface energy term,

which is analogous to the theory of nucleation.⁵⁴ A practical value in silicon is estimated¹⁷ to be $c = 1 \text{ mm}$, based on the estimated values of $\gamma \approx 1 \text{ J/m}^2$, $\sigma \approx 10 \text{ MPa}$ and $E \approx 100 \text{ GPa}$. On the other hand, the theory of linear elasticity gives a divergent stress tensor at the local crack tip region;

$$\sigma_{ij} \approx \frac{K}{\sqrt{2\pi r}}. \quad (\text{A2})$$

The theory is two dimensional, as in Fig. 1(a)-(c), and r is the distance from the crack tip. In Eq. (A2), the angular dependent factor is ignored. The critical value of the factor K for cleavage, $K = K_c$, is measured experimentally. The continuum mechanics gives an estimation of $K_c \approx \sqrt{2E\gamma}$, which explains the experimental value of K_c in silicon, at least, on the order⁹. With the present estimated values of E and γ , we obtain $K_c \approx 0.4 \text{ MPa}\sqrt{\text{m}}$.

Here we point out that the theory shows a *multiscale* property or a crucial difference between the nanoscale and macroscale behaviors. The divergent stress of Eq. (A2) is obtained under the condition of $r \ll c$. The divergence means a large deformation beyond linear elasticity. With the value of $c \approx 1 \text{ mm}$, the condition of $r \ll c$ is always satisfied in a nanoscale region. In results, a nanoscale simulation for cleavage is always under a large deformation beyond linear elasticity but it does *not* mean that such a large deformation is imposed on the macroscale (experimental) sample.

We also point out that a crossover is expected on cleavage between nanoscale and macroscale samples, since the critical crack length c is derived as a quantity independent on the sample size L . In the above picture, an enough large sample size ($L > c$) is assumed. If the sample size L is about or smaller than the above critical crack length c ($L \leq c$), the fracture behavior should be different from the above picture. In the context of the analogy to the theory of nucleation, the above situation ($L \leq c$) corresponds to the nucleation under a spatial confinement. The possibility of the crossover is investigated in our previous work¹⁷ and Sections VIII in this paper.

APPENDIX B: DETAILS IN ELECTRONIC STRUCTURE CALCULATION

The practical algorithm in the present large-scale electronic structure calculation is based on an exact equation of the Wannier states¹⁵

$$H_{\text{WS}}^{(i)} |\phi_i^{(\text{WS})}\rangle - \varepsilon_i |\phi_i^{(\text{WS})}\rangle = 0 \quad (\text{B1})$$

with the one-electron energy

$$\varepsilon_i \equiv \langle \phi_i^{(\text{WS})} | H_{\text{WS}}^{(i)} | \phi_i^{(\text{WS})} \rangle = \langle \phi_i^{(\text{WS})} | H | \phi_i^{(\text{WS})} \rangle. \quad (\text{B2})$$

Here a mapped Hamiltonian $H_{\text{WS}}^{(i)}$ is introduced and is uniquely determined by the given Hamiltonian H and the

other occupied Wannier states $\{\phi_j^{(\text{WS})}\}_{j \neq i}$.¹⁵ A Wannier state $|\phi_i^{(\text{WS})}\rangle$ is not an eigen state of the original Hamiltonian H but the lowest-energy eigen state of the mapped Hamiltonian $H_{\text{WS}}^{(i)}$. Practical large-scale calculations are realized, when Eq. (B1) is solved by the first order perturbation or the variational procedure.^{15,16} The perturbation procedure is much faster than the variational procedure but its applicability is limited, as should be in a perturbation theory. The parallelism can be done with respect to the index i of Wannier states $\{\phi_i^{(\text{WS})}\}$. In the present paper, the parallelism is done by the OpenMP technique (www.openmp.org). In the bench mark of Fig. 13, the computational time of our calculations is ‘order- N ’, or linearly proportional to the system size (N). Several related methods⁴⁸ were also developed but are not used in this paper.

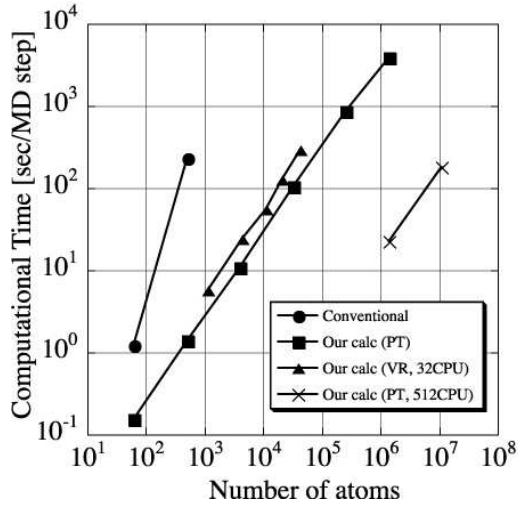


FIG. 13: The computational time for the molecular dynamics simulation with up to 11,315,021 Si atoms. Our calculations in the perturbation (PT) or variational (VR) procedure for Wannier states are compared with the conventional calculation for the eigen states. The circle or square indicates the result of the conventional method or the PT procedure, respectively, by a standard workstation.¹⁷ The triangle or cross indicates the result of the VR procedure with 32 CPUs or the PT procedure with 512 CPUs, respectively, by a parallel computation system (SGI Origin 3800TM).

All the present cleavage simulations are carried out with the variational procedure. The perturbation procedure is, however, useful in preparing the initial (non-cleaved) structures, since we can save the computational time without the use of a parallel computation system. In the cleavage simulation, a desirable initial structure is close to the critical condition for cleavage but it is non-trivial to prepare such a structure. The actual preparation is to search proper values of the parameters for the external load (See Appendix C). The perturbation procedure is applicable to non-cleaved samples, when the un-

perturbed wavefunction is chosen as the bulk (sp^3) bonding states.^{15,16,18} The parameters for the external load should be chosen *not* to grow the perturbation terms, because the growth means an undesirable large deformation, beyond linear elasticity. After determination of the appropriate parameter set for the external load, the cleavage simulation can be carried out, using the variational procedure, with a slightly larger external load and/or a point defect for cleavage ‘seed’ (See Appendix C). The resultant wavefunctions in the perturbation procedure can be chosen as the initial wavefunctions in the variational (iterative) procedure. In other words, the calculation procedure can be *seamlessly* switched from the perturbation one into the variational one. In general, every method has its own limitation in validity and it is important in practical large-scale calculations to choose or switch methods according to the purpose. This is why we have developed several different methods for large-scale calculations.^{15,16,17,18,19,20}

The technical details are explained for the present cleavage simulations with the variational procedure. The practical algorithm is to solve Eq. (B1) iteratively under explicit localization constraint on each Wannier state. The range of the localization regions affects the computational time and is *dynamically* controlled, as follows. Since the left hand side of Eq. (B1), denoted as $\delta\phi_i$, is the residual deviation from the exact solution, its norm $|\delta\phi_i|^2$ can be used as the measure of accuracy. The localization center \mathbf{r}_i of a wavefunction ϕ_i is defined and automatically updated as $\mathbf{r}_i = \langle \phi_i | \hat{\mathbf{r}} | \phi_i \rangle$. The localization center of a bulk bonding state, for example, is placed at its bond center. The cutoff radius of localization is tuned, dynamically, so that the localization region contains a given number of atoms N_i . The practical number N_i is dynamically assigned to be, typically, $N_i = 40 - 80$, according to the value of $|\delta\phi_i|^2$. If a calculated wavefunction ϕ_i gives a large value of $|\delta\phi_i|^2$, or a relatively large deviation from the exact solution, the number N_i will increase so as to relax the localization constraint and decrease the deviation. In short, the localization constraint is controlled dynamically and individually on each wavefunction, so as to keep the accuracy among various situations. The dynamical control of the localization constraint is important for a cleavage simulation, because the wavefunctions change their characters drastically and individually, in the process of bond breaking and surface reconstruction.¹⁷ More detailed explanations are described elsewhere.²⁰ It may be noteworthy that the practical system size with the variational procedure is sometimes limited by the required memory size, because all the wavefunctions and the density matrix should be stored in the memory during the calculation. For example, the required memory size with 10^4 atoms is, typically, 1.4 GB, which is close to the practical limitation of a 32-bit workstation.

APPENDIX C: DETAILS OF CLEAVAGE SIMULATION

Here we explain the technical details particular for the cleavage simulation. The time step of the molecular dynamics is 3 fs. The center of gravity of the sample is fixed as a constraint. In the present cleavage simulations, sample surfaces are terminated by orientationally fixed sp^3 bonding states. This boundary condition corresponds to the situation in which the sample is embedded in a macroscale bulk (sp^3 -bonded) system. This situation is quite different from that with the usual hydrogen termination, in which the atomic structure is deformed significantly from the tetrahedral geometry, due to the large deviation from the sp^3 bonding.

An important technique for cleavage is preparing initial defect bonds for cleavage ‘seed’; An additional short-range repulsive force is imposed on the atom pairs of selected bond sites. Since the repulsive force is of short range, it will act on nothing after the bond breaking. The repulsive forces are imposed on the bond sites near the sample surface, typically, up to the two or three bond layers from the sample surface. The seed is seen in Fig. 5(b) or Fig. 11(b).

Another important technique is imposing the external load whose physical origin is the concentrated strain field near the crack tip (See Appendix A). The external load is realized by (I) the constrained movement on sample surfaces or (II) the external force field. Now we pick out three typical cases of Fig. 3, Fig. 5 and Fig. 11. In the case of Fig. 3, the external load is imposed by the constrained movement (I). The details are the same as in Fig.2 of our previous work,¹⁷ except the absence of a cleavage seed. The absence of a seed results in multiple cleavage planes.

In Fig. 5, the external load is realized by the constrained movement (I). The atoms of the outermost two layers on the top and bottom sample surfaces are constrained under an artificial displacement in the [111] direction. Here we define the X , Y and Z axes as the $[\bar{2}11]$, $[01\bar{1}]$ and $[111]$ directions, respectively (See Fig. 5(f) for geometry). The position of the I -th atom is denoted as (X_I, Y_I, Z_I) . No constraint is imposed on the movement in the Y direction. In the ideal (crystalline) structure, the atoms are placed in the range of $0 \leq X_I \leq L_X$, $-L_Z/2 \leq Z_I \leq L_Z/2$ with the sample lengths of $L_X = 14$ nm and $L_Z = 10$ nm. The deformation of X_I is frozen ($X_I(t) = (\text{const})$). The displacement in the Z axis from the ideal (crystalline) position is given, for $t > 0$, as

$$\delta Z_I(t) = \min\{u_{\text{ini}} + (L_X - X_I) \tan \alpha t, u_{\text{max}}\}, \quad (\text{C1})$$

where u_{max} , u_{ini} , α are constants. The directions of the displacement are opposite on the top and bottom sample surfaces for the ‘opening’ motion, as seen in Fig. 5. At $t < 0$, the displacement is uniform ($\delta Z_I(t) = u_{\text{ini}}$). Among the atoms near the right edges on the top and bottom sample surfaces ($X_I \approx L_X$), the displacement is nearly

fixed ($\delta Z_I(t) \approx u_{\text{ini}}$), during the opening motion ($t > 0$). In other words, the length of the right sample edge in Fig.5 is preserved.

The parameters, u_{ini} , u_{max} and α , are chosen so as to simulate the stable cleavage propagation on single (111) cleavage plane; (a) The parameter u_{ini} , the parallel displacement of the initial structure ($t = 0$), is determined so that the cleavage does *not* occur without the opening motion, even if the parallel gap by u_{ini} is introduced between successive two atom layers. With a too large value of u_{ini} , the cleavage begins with multiple cleavage planes. With a too small value of u_{ini} , a large opening angle is required for cleavage, which may cause a too large deformation in the left most edge on the upper and bottom sample surfaces. In the case of Fig.5, the value is chosen as $u_{\text{ini}} \approx 0.6$ Å as a typical one. The sample length increases from L_Z into $L_Z + 2u_{\text{ini}}$ but the modification is only $2u_{\text{ini}}/L_Z \approx 1\%$. (b) The maximum displacement u_{max} is introduced so as to prevent a large deformation at the left edges on the top and bottom sample surfaces. Such a large deformation at the edges will result in multiple cleavage planes. In the case of Fig.5, the value is chosen as $u_{\text{max}} \approx 1.0$ nm as a typical one. In the case of Fig.5(d), almost the half area is flat on the top and bottom sample surfaces, where the atoms reach the maximum deformation ($\delta Z_I(t) = u_{\text{max}}$). (c) The parameter α governs the opening motion as the velocity of ‘opening angle’. Using the mathematical relation $\tan \alpha t \approx \alpha t$ for a small angle of αt , each atoms are under the constant velocity motion with the velocity of $V_I \equiv (L_X - X_I)\alpha$. The maximum velocity appears at the left edges of the top and bottom sample surfaces ($X_I \approx 0$, $Z_I \approx \pm L_Z/2$) and is given as $v_0 \equiv L_X\alpha$. Since the cleavage propagation velocity is on the order of the Rayleigh wave velocity $v_R = 4.5$ km/s, the velocity v_0 should be much slower than the Rayleigh wave velocity ($v_0 \ll v_R$). With a too fast velocity of v_0 , the atoms in the constraint motion, (the atoms on the top and bottom sample surfaces) are removed from the sample and no internal (cleavage) surface appears. With a too slow velocity of v_0 , the simulation wastes the computational time before the beginning of cleavage. In the case of Fig.5, we choose $v_0 = 0.16$ km/s = 0.16 nm/ps, as a typical value.

Now we turn to explain the case of Fig. 11, in which the external load is realized by an external force field (II) on selected atoms. The selected atoms are within several layers near the sample surfaces, except the left one. The thickness of the layers is 5 % of the sample length on the top or bottom surface and 10 % on the right surface. For a selected atom at the (two-dimensional) coordinate $\mathbf{r} \equiv (X, Z)$, the external force

$$\mathbf{F}(\mathbf{r}) = \frac{Kd_0^2}{\sqrt{2\pi r}} \frac{\mathbf{r}}{|\mathbf{r}|} \quad (\text{C2})$$

is imposed. The force center $\mathbf{r} = 0$ is fixed at the position of the initial defect and is placed almost at the middle of the left sample surface. The above expression is given by integration of the stress in Eq. (A2) on the

area of d_0^2 . The length d_0 should be a typical length scale for one atom. In the present paper, the practical value of d_0 is determined so that the volume per atom is d_0^3 ($d_0 \approx 3\text{\AA}$). We can expect that the cleavage will occur, when the factor K is on the order of the critical value K_c that is estimated in Appendix A ($K \approx K_c$). In Fig. 11, the value of K is chosen as $K \approx 2K_c$. In several other simulations, the external force field is given with a movement of the force center, according to the fact that the crack tip moves with the cleavage propagation. We do not find, however, a systematic difference on the resultant cleavage behavior.

Finally, we explain controlling the total kinetic energy in Fig. 5 and Fig. 11. The total kinetic energy is controlled by the Nosé thermostat method.⁵⁵ The temperature parameter of the thermostat is set to be $T=800\text{K}$, as a typical value. The temperature parameter T , however, does *not* correspond to an experimental temperature, since the present simulation is a non-equilibrium process. The appropriate choice of the value of T is es-

sential, especially, in the case of Fig. 5, in which a deformation is introduced on the sample surfaces by the constraint movement with the characteristic velocity of v_0 . The temperature parameter T should be enough large so as to propagate the introduced deformation into the internal region.

ACKNOWLEDGMENTS

We thank Yutaka Mera, Kouji Maeda and Masakazu Ichikawa (University of Tokyo) for discussion on experiments. Numerical calculation is partly carried out with the facilities of Japan Atomic Energy Research Institute and of Institute for Solid State Physics, University of Tokyo. This work is financially supported by ‘Research and Development for Applying advanced Computational Science and Technology’ of Japan Science and Technology Corporation.

¹ A. A. Griffith, Philos. Trans. R. Soc. London, Ser. A **221**, 163 (1920).

² N. F. Mott, Engineering **165**, 16 (1948).

³ As general references of brittle fracture, L. B. Freund, ‘Dynamic fracture mechanics’, Cambridge university press (1989); B. Lawn, ‘Fracture of brittle solids’, 2nd ed., Cambridge university press (1993).

⁴ As a review, H. Neddermeyer, Rep. Prog. Phys. **59**, 701 (1996).

⁵ K. C. Pandey, Phys. Rev. Lett. **47**, 1913 (1981).

⁶ J. E. Northrup and M. L. Cohen, Phys. Rev. Lett. **49**, 1349 (1982).

⁷ F. Ancilotto, W. Andreoni, A. Selloni, R. Car, and M. Parrinello, Phys. Rev. Lett. **65**, 3148 (1990).

⁸ Y. M. Huang, J. C. H. Spence, O. F. Sankey, and G. B. Adams, Surf. Sci. **256**, 344 (1991).

⁹ J. C. H. Spence, Y. M. Huang, and O. Sankey, Acta Metall. Mater. **41**, 2815 (1993).

¹⁰ M. Rohlfing and S. G. Louie, Phys. Rev. Lett. **83**, 856 (1999).

¹¹ See the following recent work or references therein; A. A. Stekolnikov, J. Furthmüller, and F. Bechstedt, Phys. Rev. B **65**, 115318 (2002).

¹² M. Henzler, Surf. Sci. **36**, 109 (1973).

¹³ M. A. Lutz, R. M. Feenstra, and J. O. Chu, Surf. Sci. **328**, 215 (1995).

¹⁴ R. Pérez and P. Gumbsch, Phys. Rev. Lett. **84**, 5347 (2000).

¹⁵ T. Hoshi and T. Fujiwara, J. Phys. Soc. Jpn. **69**, 3773 (2000).

¹⁶ T. Hoshi and T. Fujiwara, Surf. Sci. **493**, 659 (2001).

¹⁷ T. Hoshi and T. Fujiwara, J. Phys. Soc. Jpn. **72**, 2429 (2003).

¹⁸ M. Geshi, T. Hoshi, and T. Fujiwara, J. Phys. Soc. Jpn. **72**, 2880 (2003).

¹⁹ R. Takayama, T. Hoshi, and T. Fujiwara, J. Phys. Soc. Jpn. **73**, 1519 (2004).

²⁰ T. Hoshi, D. Thesis, School of engineering, University of Tokyo (2003); T. Hoshi, unpublished.

²¹ W. Kohn, Phys. Rev. B **7**, 4388 (1973).

²² W. Kohn, Chem. Phys. Lett. **208**, 167 (1993).

²³ I. Kwon, R. Biswas, C. Z. Wang, K. M. Ho, and C. M. Soukoulis, Phys. Rev. B **49**, 7242 (1994).

²⁴ J. C. Phillips, Rev. Mod. Phys. **42**, 317 (1970).

²⁵ W. A. Harrison, *Electronic structure and the properties of solids*, W. H. Freeman and Company, San Francisco (1980).

²⁶ P. Vogl, H. P. Hjalmarsson, and J. D. Dow, J. Phys. Chem. Solids **44**, 365 (1983).

²⁷ O. K. Andersen, O. Jepsen, and D. Glötzel, in *Highlights of condensed matter theory*, North Holland (1985).

²⁸ O. K. Andersen, T. Saha-Dasgupta, R. W. Tank, C. Arcangeli, O. Jepsen, and G. Krier, in *Electronic Structure and Physical Properties of Solids. The Uses of the LMTO Method*, Ed. H. Dreysse, Springer-Verlag, Berlin, 3 (2000).

²⁹ O. K. Andersen, T. Saha-Dasgupta, and S. Ezhov, Bull. Mater. Sci. **26**, 19 (2003).

³⁰ C. H. Xu, C. Z. Wang, C. T. Chan, and K. M. Ho, J. Phys. Condens. Matter **4**, 6047 (1992).

³¹ See Refs.^{15,16} and references therein.

³² A simple way for the distinction of the electronic structures between Si and Ge is given by the introduction of an extra spherical orbital, so called ‘ s^* ’ orbital, as well as the s and p orbitals.²⁶ The physical origin of the extra orbit is the five d orbitals. Such a description is essential for the conduction band and was used, for example, in a calculation of optical properties of Si(001) surfaces; A. I. Shkrebtii and R. Del Sole, Phys. Rev. Lett. **70**, 2645 (1993). See also an *ab initio* work,²⁹ in which a recent formulation with muffin-tin orbitals is applied to Si case. These works may be important, when one would like to describe the electronic structure beyond the present Hamiltonian.

³³ D. J. Chadi, Phys. Rev. Lett. **43**, 43 (1979).

³⁴ P. Krüger and J. Pollmann, Phys. Rev. Lett. **74**, 1155 (1995).

³⁵ In the present paper, we do not focus the difference of the (111)-(2 \times 1) structures between Si and Ge surfaces. The

difference can be seen with fine experimental and theoretical works. See, for example, H. Hirayama, N. Sugihara and K. Takayanagi, Phys. Rev. B **62**, 6900 (2000); M. Rohlffing, M. Palummo, G. Onida and R. Del Sole, Phys. Rev. Lett. **85**, 5440 (2000).

³⁶ In silicon case, the surface energy of 1 J/m² is the order of 1 eV per surface atom, which is a typical energy scale of chemical process.

³⁷ C.-C. Fu, M. Weissmann, and A. Saúl, Surf. Sci. **494**, 119 (2001).

³⁸ Surface energy of several *ideal* surfaces can be explained by the number of broken bond sites per unit area. For example, the number of broken bond sites on the (111) surface is smaller than that on the (001) surface, which explains the fact that the surface energy of the *ideal* Si(111) surface is smaller than that of the *ideal* Si(001) surface ($\gamma_{(001)}^{\text{ideal}} = 2.39 \text{ J/m}^2$, $\gamma_{(111)}^{\text{ideal}} = 1.82 \text{ J/m}^2$).¹¹ As discussed in the text, this simple explanation is not valid for the *reconstructed* silicon surfaces.

³⁹ O. L. Alerhand, D. Vanderbilt, R. D. Meade, and J. D. Joannopoulos, Phys. Rev. Lett. **61**, 1973 (1988); O. L. Alerhand, A. N. Berker, J. D. Joannopoulos, D. Vanderbilt, R. J. Hamers, and J. E. Demuth, Phys. Rev. Lett. **64**, 2406 (1990).

⁴⁰ For a review, H. J. W. Zandvliet, Rev. Mod. Phys. **72**, 593 (2000).

⁴¹ As a common tendency among the surface structures on Si or Ge, the upper (vacuum side) atom has an *excess* population and the lower (bulk side) one has an *deficit* population. A example is also seen in the asymmetric dimer on (001) surface shown in Fig. 3(f). The fact can be explained from the hybridization freedom.³³ The tendency is seen in other examples, such as the bucked and π -bonded (111)-(2 \times 1) structures (See Section V A or literatures such as Ref.¹⁰). A semi-qualitative explanation is as follows: A (111) surface atom with a deficit population, is expected to form a graphite-like flattened structure, like the C atom site in Fig. 6(e), since the electron system should be similar to the sp^2 hybridization, rather than the sp^3 hybridization.

⁴² Y. Mera, T. Hashizume, K. Maeda, and T. Sakurai, Ultramicroscopy **42-44**, 915 (1992).

⁴³ D. Haneman, Phys. Rev. **121**, 1093 (1961).

⁴⁴ See a recent theoretical investigation,¹⁰ in which the two tilted structures are compared, as the flat surfaces (without a crack tip), beyond the standard *ab initio* (LDA) theory. See also the Ge case.³⁵

⁴⁵ R. M. Feenstra and J. A. Stroscio, Phys. Rev. Lett. **59**, 2173 (1987).

⁴⁶ H. Tokumoto, S. Wakayama, K. Miki, H. Murakami, S. Okayama, and K. Kajimura, J. Vac. Sci. Technol. B **9** 695 (1991); T. Komeda, S. Gwo, and H. Tokumoto, Jpn. J. Appl. Phys. **35**, 3724 (1996).

⁴⁷ D. J. Chadi and J. R. Chelikowsky, Phys. Rev. B **24**, 4892 (1981).

⁴⁸ For example, a hybrid scheme within quantum mechanics gave a simulation of 10^5 Si atoms,^{17,20} in which the perturbation and variational procedures are used simultaneously in one sample.

⁴⁹ Yutaka Mera, private communication.

⁵⁰ Masakazu Ichikawa, private communication.

⁵¹ K. Fujita, Y. Kusumi, and M. Ichikawa, Surf. Sci. **357-358**, 490 (1996).

⁵² A. A. Shklyaev and M. Ichikawa, Phys. Rev. B **65** 045307 (2002).

⁵³ International Technology Roadmap for Semiconductors, <http://public.itrs.net>.

⁵⁴ For example, L. D. Landau and E. M. Lifshitz: *Statistical Physics*, Pergamon Press, Oxford, (1980) 3rd ed., Part I.

⁵⁵ S. Nosé, Mol. Phys. **52**, 255 (1984); W. G. Hoover, Phys. Rev. A **31**, 1695 (1985).